Journal of
Materials Chemistry A

ROYAL SOCIETY
OF CHEMISTRY

PAPER

View Article Online
View Journal | View Issue

Cite this: *J. Mater. Chem. A*, 2025, **13**, 21063

Electrochemical nitrate reduction to ammonia using laser-processed Nb_2AlC: the role of effective Al etching†

Shaista Nouseen,[ab] Sujit Deshmukh,[b] Michal Langer,[c] Michal Otyepka [cd]
and Martin Pumera *[abefg]

Electrocatalytic nitrate reduction reaction to ammonia (NH_3) is a promising approach for generating NH_3 compared with the widely used Haber–Bosch process. It offers the advantage of zero carbon emission and helps in recycling nitrate waste. However, the challenge remains in the synthesis and engineering of proficient electrocatalytic materials with high faradaic efficiency and yield rate. Herein, we report a unique laser-processed niobium oxide-graphene (NbO_x-Gr) electrode attached to a conductive support of graphene for NH_3 generation. The two-step fabrication process started with spatially and temporally controlled pulsed laser writing on an Nb_2AlC-coated polymer surface followed by simple electrochemical etching to remove excess Al. Electrochemical analysis elucidated that the NbO_x-Gr electrode exhibited improved activity for ammonia generation. Moreover, theoretical studies provide insights into the nitrate reduction reaction mechanism, confirming that the electrochemical active site was located on the Nb atom of the NbO_x-Gr electrode. Laser processing is a cost-effective, less chemically hazardous, versatile, and efficient approach to utilize MAX phases for multiple energy storage and conversion applications.

Received 25th March 2025
Accepted 13th May 2025

DOI: 10.1039/d5ta02418h

rsc.li/materials-a

1 Introduction

Ammonia (NH_3) is an indispensable industrial-scale chemical feedstock used in the agriculture industry; it is a hydrogen-rich and carbon-free fuel and has environmentally friendly nature.[1–3] The industrial-scale synthesis of NH_3 is largely dependent on the Haber–Bosch process. While millions of tonnes of NH_3 are produced annually through the Haber–Bosch process,[2–8] it consumes 1–2% of global energy and contributes to 1.0% of global carbon emissions, elevating environmental hazards.[9–11] Another conventional approach involves nitrogen (N_2) reduction to NH_3, where water molecules act as proton sources. Nevertheless, the intrinsic properties of the N_2 molecule, like high $N \equiv N$ bond dissociation energy of 941 kJ mol^{-1} and low solubility in water, negatively impact the yield rate and selectivity of the N_2 to NH_3 conversion process.[10–15] Thus, developing more sustainable approaches for NH_3 production have recently gained significant research interest.

In this direction, the electrocatalytic nitrate reduction reaction, $NO_3^- + 6H_2O + 8e^- \rightarrow NH_3^+ + 9OH^-$, has high potential as it offers a sustainable route and provides a plethora of advantages such as (i) less environmental impact and high feedstock availability, *i.e.*, nitrate (NO_3^-) ions are produced as agricultural fertilizers and industrial waste;[15–17] this waste can be utilized for NH_3 generation, making this route environmentally friendly while simultaneously remedying nitrate waste, (ii) high energy efficiency: NO_3^- reduction to ammonia consumes less energy as the dissociation energy for $N{=}O$ in the NO_3^- ion is approximately 204 kJ mol^{-1}, which is lesser compared to other approaches, (iii) high solubility: the solubility of the NO_3^- ion (880 g L^{-1}) in H_2O is superior compared to of N_2 (0.02 g L^{-1}).[15–20]

Thus, the adsorption of the NO_3^- ions on the electrocatalyst surface is more efficient, leading to enhanced electrochemical performance.[21,22] However, a major obstacle in producing ammonia from NO_3^- ions is the competing hydrogen evolution

---

[a] *Quantum Materials Laboratory, 3D Printing & Innovation Hub, Center for Nanorobotics and Machine Intelligence, Department of Chemistry and Biochemistry, Mendel University in Brno, Zemedelska 1, Brno 61300, Czech Republic. E-mail: pumera.research@gmail.com*

[b] *Future Energy and Innovation Laboratory, Central European Institute of Technology, Brno University of Technology, Purkynova 123, Brno 61200, Czech Republic*

[c] *IT4Innovations, VŠB – Technical University of Ostrava, 17. listopadu 2172/15, Poruba 70800, Ostrava, Czech Republic*

[d] *Czech Advanced Technology and Research Institute (CATRIN), Regional Centre of Advanced Technologies and Materials, Palacký University Olomouc, Šlechtitelů 27, Olomouc, 77900, Czech Republic*

[e] *Advanced Nanorobots and Multiscale Robotics Laboratory, Faculty of Electrical Engineering and Computer Science, VSB - Technical University of Ostrava, 17. listopadu 2172/15, Ostrava 70800, Czech Republic*

[f] *Department of Medical Research, China Medical University Hospital, China Medical University, No. 91 Hsueh-Shih Road, Taichung, Taiwan*

[g] *Department of Chemical and Biomolecular Engineering, Yonsei University, 50 Yonsei-ro, Seodaemun-gu, Seoul, 03722, Korea*

† Electronic supplementary information (ESI) available. See DOI: **https://doi.org/10.1039/d5ta02418h**

reaction (HER), leading to lower faradaic efficiency.[23,24] Currently, noble and non-noble metal-based electrocatalysts,[25] such as Pt–TiO_2,[26] copper-based catalysts,[27] metal oxides,[28] and 2D materials,[29] have been explored as electroactive materials for the nitrate reduction reaction. Nevertheless, these electrocatalyst materials face some limitations, such as high cost, low abundance, susceptibility to leaching, and predominance of the HER at high potentials.[30–32] Therefore, developing new electrocatalyst materials for the effective conversion of NO_3^- into NH_3 is crucial.

In this context, ternary-layered MAX phases with their unique blend of metallic and ceramic properties, along with high thermal stability and a combination of covalent and metallic bonds, offer substantial potential for electrochemical energy conversion applications.[33,34] Typically, MAX phases are employed to fabricate MXenes by removing aluminium layers using hazardous acids (HF).[35] Thus, HF-free approaches are gaining significant attention.[36] It is noteworthy here that recently MAX phases have gained significant attention for energy applications.[37] However, MAX phases for electrocatalytic nitrate reduction reactions have not been reported. The major obstacles in this context are tuning their electrical properties and removing aluminium layers to fabricate a well-ordered architecture that utilizes the full potential of MAX phases.[33–38] To resolve these issues, heterostructure engineering,[39] interface engineering,[40] and doping approach[41] have been explored to enhance the electrochemical performance of MAX phases.[42–44]

Herein, we reported a versatile, single-step, cost-effective, less chemically hazardous laser processing approach for fabricating the heterostructures of MAX (Nb_2AlC) with graphene.[45] This involves a single-step laser processing of Nb_2AlC decorated over graphene. Subsequently, to eradicate the aluminium content from the laser-processed Nb_2AlC, an electrochemical etching approach is employed. The fabricated Nb matrix-loaded graphene (NbO_x-Gr) electrodes were employed for electrocatalytic nitrate reduction reaction to generate NH_3. This approach to fabricate NbO_x-Gr electrode using Nb_2AlC-coated PI, employing laser treatment followed by electrochemical etching enables the utilisation of MAX phases more efficiently without the use of hazardous HF and opens the door for exploring a broad range of different MAX phases and other 2D materials integrated with graphene for diverse applications beyond energy conversion and storage applications.

2 Results and discussion

2.1 Fabrication process

First Nb_2AlC-coated polyimide sheets are subjected to laser irradiation using a diode-pumped Nd:YAG solid pulsed laser beam (532 nm), generating niobium-based spherical nanoparticle decorated over graphene thin films. The high-energy laser pulses create substantial mechanical stress and thermal shock on the stacked 2D Nb_2AlC nanosheets, leading to the formation of small fragments of NbO_x spherical nanoparticles. Concurrently, the infrared energy is absorbed by the PI sheet, generating a temperature exceeding 2000 K within a millisecond range, enabling the photothermal transformation of the polyimide into graphene (Fig. 1a).

In the subsequent step, an electrochemical etching route is employed to eliminate the excess aluminium metal using the chronoamperometry method with 3 M HCl as an electrolyte in a three-electrode setup. The chloride ions (Cl^-) ions in the HCl electrolyte react with the Al in the fragmented Nb_2AlC and form aluminium chloride ($AlCl_3$).[46,47] Nonetheless, compared to the traditional approach, this process eliminates the reliance on toxic and hazardous HF-based compounds, while maximizing the usage of the MAX phase efficiently (Fig. 1b). The details of the fabrication process are outlined in the experimental section.

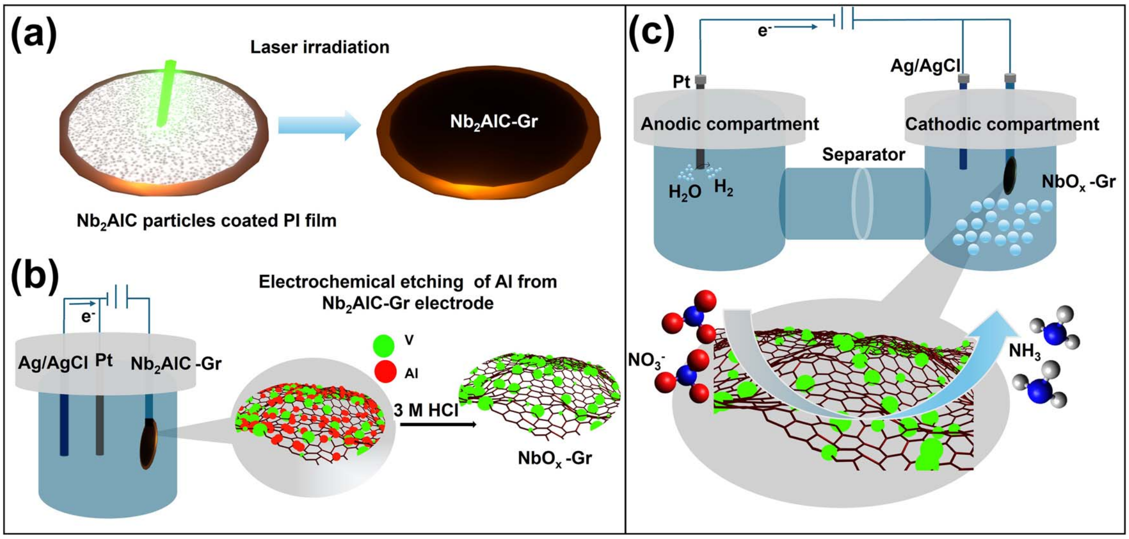

Fig. 1 (a) Schematic of the conversion of the Nb_2AlC-coated polyimide sheet into Nb_2AlC-graphene electrodes through laser processing. (b) Subsequent *in situ* electrochemical etching of the Nb_2AlC-Gr electrode in 3 M HCl electrolyte. (c) Nitrate reduction to generate ammonia using a three-electrode setup with the NbO_x-Gr electrode.

In the application context, the electrocatalytic nitrate reduction reaction to generate NH_3 was carried out using a three-electrode set-up employing an H-type electrolytic cell with a frit separation. In the three-electrode setup, Gr, Nb_2AlC-Gr, and NbO_x-Gr are employed as the working electrode, Platinum (Pt) as the counter electrode and Ag/AgCl as the reference electrode utilizing 0.5 M Na_2SO_4 as the electrolyte and 0.1 M KNO_3 as the nitrate source (Fig. 1c). We investigated the physical and chemical composition, followed by morphological analysis of these electrodes in the following sections.

Table 1 Influence of varying time of *in situ* electrochemical etching on element composition in atomic (%) (obtained from XPS survey spectra)

Samples	Nb (at%)	Al (at%)	C (at%)	O (at%)
Commercial-Nb_2AlC	10.31	8.66	40.35	40.69
Nb_2AlC-Gr	1.09	0.39	88.50	10.02
Nb_2AlC-Gr-6 h	1.03	—	90.83	8.14
Nb_2AlC-Gr-12 h	1.61	—	89.88	8.52
Nb_2AlC-Gr-18 h	2.84	—	84.18	12.98
Nb_2AlC-Gr-24 h/NbO_x-Gr	2.90	—	86.64	10.45

2.2 Material characterization

To investigate the material composition analysis and to select suitable electrodes after electrochemical etching for the electrochemical application, X-ray photoelectron spectrum (XPS) analysis was carried out. Wide survey spectrum analysis was employed to confirm the effectiveness of the etching process and to select the appropriate electrodes for the electrochemical analysis. To enable a comprehensive comparison of aluminium removal we varied the etching time (6, 12, 18, and 24 hours) during the electrochemical etching process. XPS analysis of each electrode was carried out to verify the efficiency of Al removal with varying etching times.

Note that laser-treated electrochemically etched electrodes only displayed peaks for Nb 3d, C 1s, and O 1s, indicating the effective removal of aluminium from the electrode surface (Fig. 2a). The extracted elemental composition information in atomic percentages from XPS survey spectra is provided in Table 1, which shows that aluminium accounted for 8.66% in the commercial Nb_2AlC sample, 0.39% in the Nb_2AlC-Gr electrode, and was undetectable in the electrochemically etched electrodes. This validates the effectiveness of aluminium removal through the *in situ* electrochemical etching process.

Before testing the electrodes for the electrochemical application, the selection of the appropriate electrochemically etched electrode for the nitrate reduction to ammonia is essential. Thus, we performed linear sweep voltammetry (LSV) measurements in a three-electrode setup employing 0.5 M Na_2SO_4 as the electrolyte, as illustrated in Fig. S1 in ESI.† We observed that the NbO_x-Gr electrode subjected to the etching process for 24 h exhibited enhanced electrochemical performance compared to the Nb_2AlC-Gr, and other etching time variants (6 h, 12 h, and 18 h). Thus, we selected the NbO_x-Gr-24 h. electrode for further investigation, and we named the electrode NbO_x-Gr throughout the manuscript.

X-ray diffraction (XRD) patterns were acquired to investigate the phase transition of the commercial-Nb_2AlC, Gr, Nb_2AlC-Gr, and NbO_x-Gr electrodes as illustrated in Fig. 2b. The diffraction peaks detected for the commercial-Nb_2AlC powder correspond closely to those previously reported Nb_2AlC MAX phases, indicating the absence of impurities.[48] The Gr demonstrated a characteristic graphene peak and additional peaks corresponding to the PI substrate.[49] The (002) peak associated with Nb_2AlC disappeared in the Nb_2AlC-Gr electrode, indicating a phase transformation induced by laser treatment. Likewise, in the NbO_x-Gr electrode, the (002) peak was absent, and it exhibited new peaks, potentially corresponding to the niobium oxide composite with graphene formed after the electrochemical etching treatment.[50] The XRD pattern confirms the phase transformation of the Nb_2AlC MAX phase.

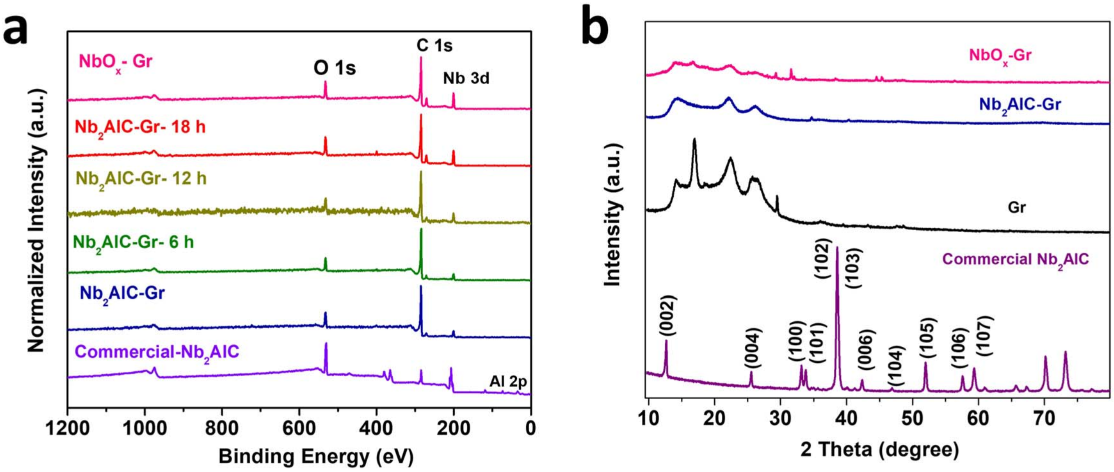

Fig. 2 Physical characterization of commercial Nb_2AlC powder, Gr, Nb_2AlC-Gr and NbO_x-Gr electrodes. (a) XPS survey spectra demonstrating the time-dependent electrochemical etching of Al metal. Commercial Nb_2AlC powder was compared with Nb_2AlC-Gr, Nb_2AlC-Gr-6 h, Nb_2AlC-Gr-12 h, Nb_2AlC-Gr-18 h, and NbO_x-Gr electrodes. (b) XRD spectra of commercial Nb_2AlC powder, Gr, Nb_2AlC-Gr, and NbO_x-Gr electrodes.

We utilized Raman spectroscopy to correlate the phase transformation findings observed in the XRD measurements and to investigate the changes in the Gr, Nb_2AlC-Gr, and NbO_x-Gr electrodes. The outcome reveals that two Raman-active E_{2g} and A_{1g} optical modes of the Nb_2AlC MAX phase are absent in the Nb_2AlC-Gr and NbO_x-Gr electrode samples, as illustrated in Fig. S2a–c.† According to the existing literature, the E_{2g} optical mode (theoretical value ≈ 181.5 cm^{-1}) corresponds to the Nb and C atoms' in-plane oscillations, coupled with minor contributions from Al atom oscillations. The observed suppression of the E_{2g} mode could be attributed to the substitution of the Al atom with lighter O atoms. The absence of the A_{1g} optical mode (theoretical value ≈ 262.8 cm^{-1}) corresponds to the Nb and C atom's symmetric vibrations out-of-plane and could be associated with an expansion in layer spacing.[51–53] In our case the A_{1g} optical mode could undergo a shape transformation and downshift due to the laser and etching treatment. The suppression of the optical mode in the Nb_2AlC-Gr and NbO_x-Gr electrodes confirms the etching of Al and phase transformation, corroborated by the XRD measurements.[51–53] Besides, after the laser treatment, the intensity of D bands does not have a significant difference in the Gr and Nb_2AlC-Gr samples. However, the D band in the NbO_x-Gr increased after electrochemical etching, while the intensity of the G band decreased, which indicates an increase in defects. We also determined the coherence length (L_a) of the graphene layered structure along *ab* planes (see details in the ESI†). The coherence lengths of NbO_x-Gr, Nb_2AlC-Gr, and Gr electrodes are 16.31 nm, 21.40 nm, and 22.97 nm, respectively. This trend in coherence length implies that crystallinity is crippled along the *ab* planes.[54] Additionally, the Raman spectra of pristine polyimide sheets are provided,[55] to confirm the successful conversion of polyimide sheets into graphene (Fig. S2b†).

XRD and Raman measurements display substantial alterations in the surface chemical compositions of Nb_2AlC-Gr and NbO_x-Gr electrodes following laser exposure and subsequent etching treatment. To validate these surface chemical composition modulations, high-resolution XPS spectra of laser treated and electrochemically etched electrodes both were recorded. To better analyze the chemical bonding environment and oxidation state of the elements and to reveal the chemical transformations in the chemical composition of the Nb_2AlC-Gr electrode induced by the laser processing, individual XPS spectrum analysis for Nb 3d, Al 2p, C 1s, and O 1s was carried out. The Nb 3d high-resolution spectrum displays a doublet, with peaks at ≈ 207 eV corresponding to Nb–O $3d_{5/2}$ and ≈ 210 eV to Nb–O $3d_{3/2}$, confirming the presence of Nb_2O_5 and the Nb^{5+} oxidation state, as illustrated in Fig. 3a.[56–59] Additionally, the chemical transformation of the Nb_2AlC MAX phase is confirmed in the laser treated Nb_2AlC-Gr electrode due to the absence of the metal-carbide bond.[58,59] The detailed analysis of the C 1s spectrum illustrated in Fig. 3b shows the presence of distinct types of carbon bonds like the C–C sp^2 bond at ≈ 284.0 eV, C–C sp^3 bond at ≈ 285.0 eV, and C–O bond at ≈ 286.0 eV, like those in the Nb_2AlC MAX phase.[52,53,59] However, the absence of the Nb–C bond peak in the ≈ 282.3 eV region compared to the Nb_2AlC MAX phase confirms a chemical composition transformation of the Nb_2AlC phase induced by the laser processing.[56–60]

The high-resolution Al 2p spectrum was recorded as illustrated in Fig. 3c for the Nb_2AlC-Gr electrode. A peak is detected in the ≈ 75.0 eV region, indicating the presence of oxides of

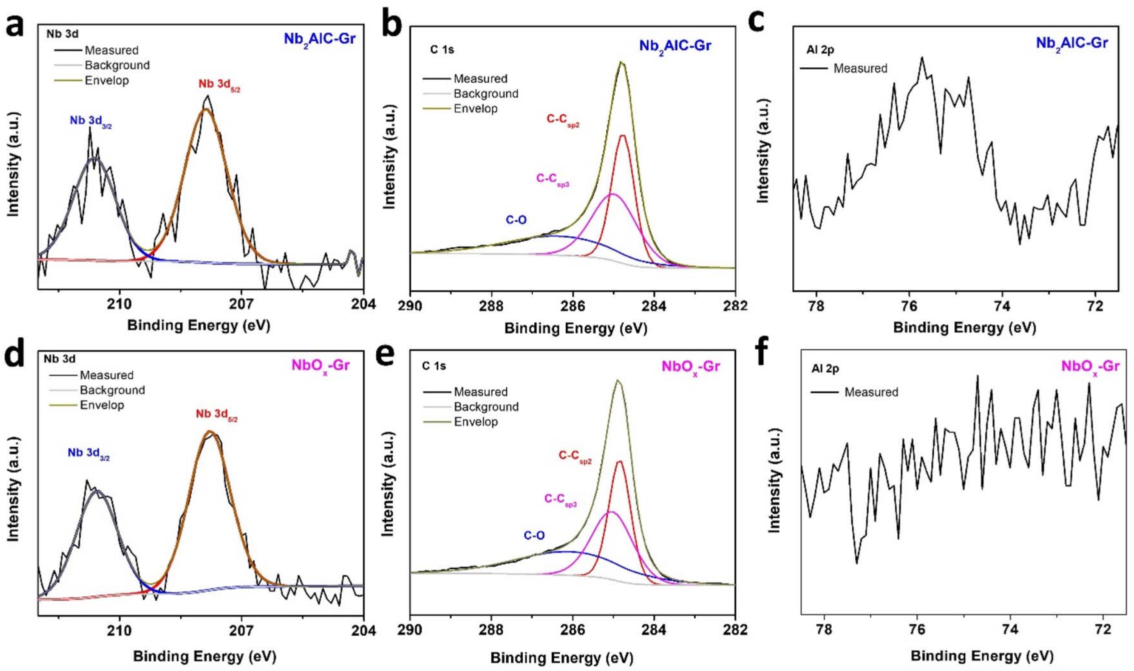

Fig. 3 Chemical composition analysis: high-resolution XPS analysis of Nb_2AlC-Gr and NbO_x-Gr electrodes. (a and d) Nb 3d, (b and e) C 1s, and (c and f) Al 2p spectra, respectively.

Al.[52,53,59] Additionally, the O 1s spectrum is provided in Fig. S3a in the ESI,† confirming the presence of all requisite elements in the Nb_2AlC-Gr electrode.[56–60] For NbO_x-Gr the Nb 3d core level spectrum exhibits doublet peaks, reflecting ≈207.0 eV for Nb–O $3d_{5/2}$ and ≈210.0 eV for Nb–O $3d_{3/2}$, indicating the existence of the Nb^{5+} oxidation state in Nb_2O_5 as shown in Fig. 3d.[56–60] These results indicate that the Nb 3d chemical composition remains unchanged relative to the laser-processed Nb_2AlC-Gr electrode.

The in-depth analysis of the carbon C 1s spectrum of the NbO_x-Gr electrode as illustrated in Fig. 3e shows similar findings compared to the C 1s spectrum of the Nb_2AlC-Gr electrode, the carbon bonds like the C–C sp^2 bond at ≈284 eV, C–Csp^3 bond at ≈285 eV, and C–O bond at ≈286.[56–59] The core level Al 2p spectrum, shown in Fig. 2f, confirms the absence of oxides of Al; this indicates the effective removal of Al through the electrochemical etching process. Fig. S3b in the ESI† exhibits the O 1s high-resolution spectra of the NbO_x-Gr electrode. The findings from the XPS measurements corroborate the results of the XRD and Raman measurements, suggesting that laser processing modifies the chemical composition of the Nb_2AlC phase, and the laser processing with the *in situ* electrochemical etching successfully removes the excess of oxides of Al from the surface of the electrodes.

The scanning electron microscopy (SEM) micrographs of the Gr, Nb_2AlC-Gr, and NbO_x-Gr electrodes are displayed in Fig. 4, where the successful integration of the Nb-rich spherical

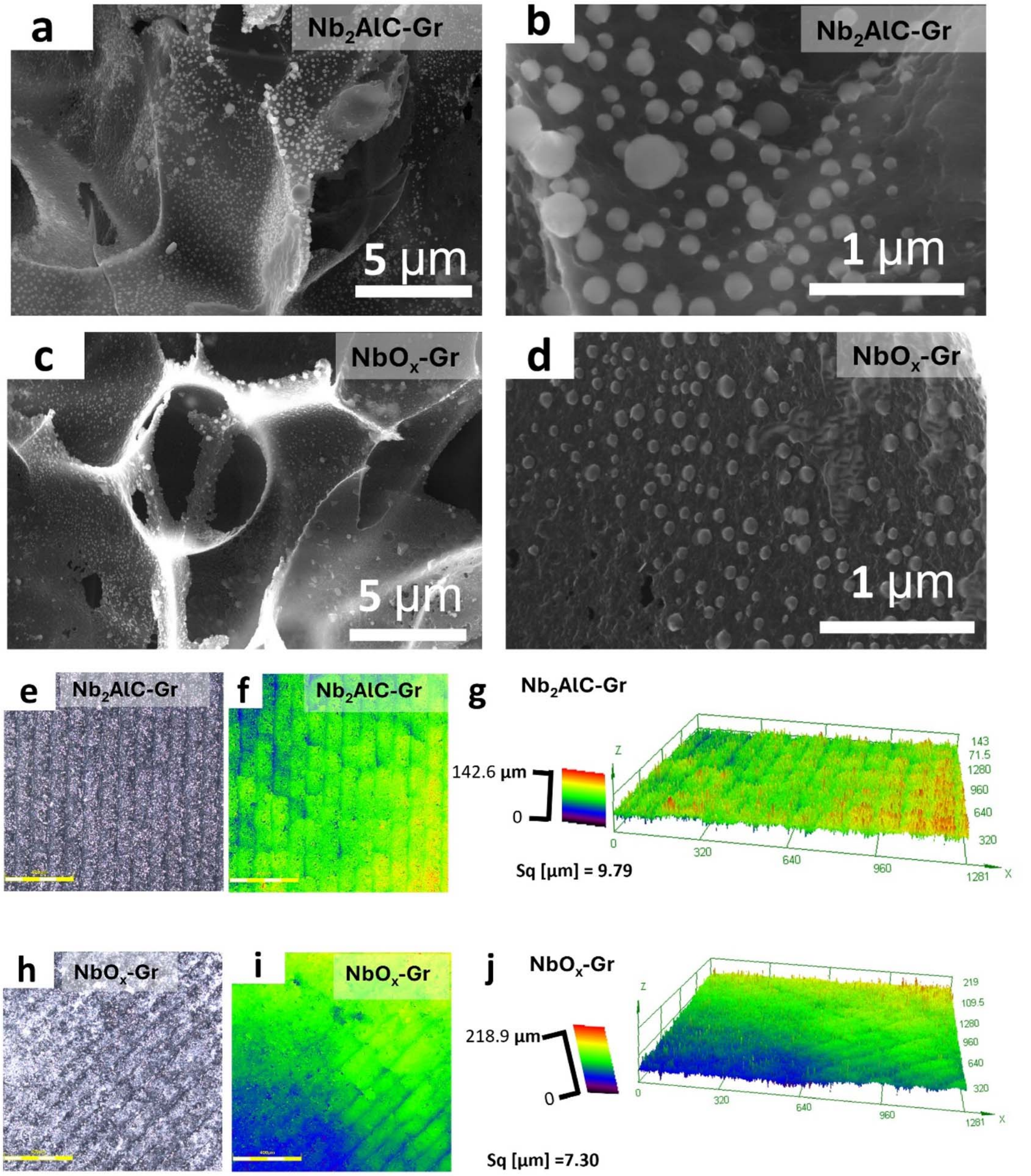

Fig. 4 Morphological characterization of Nb_2AlC-Gr and NbO_x-Gr electrodes. SEM micrographs of Nb_2AlC-Gr electrode at (a) low and (b) high magnifications, NbO_x-Gr electrode at (c) low and (d) high magnifications. CLSM optical images and collective 2D and 3D false colour mapping images of (e–g) Nb_2AlC-Gr electrode and (h–j) NbO_x-Gr electrode; scale bar ∼400 µm.

nanoparticles onto the graphene network is visualized. In the case of the Nb_2AlC-Gr film, Nb-rich spherical nanoparticles are evenly distributed onto the graphene with particle sizes spanning from the micrometre (μm) to the sub-nanometre (nm) scale (Fig. 4a and b). Even though the SEM images of the electrochemically etched sample NbO_x-Gr elucidated a similar morphology to Nb_2AlC-Gr, the particle size has decreased in NbO_x-Gr as compared to Nb_2AlC-Gr, as displayed in Fig. 4c and d, respectively. The SEM micrographs (low and high magnification) of bare Gr are provided in the ESI in Fig. S4a and b,† elucidating the successful formation of the graphene like structure from the polyimide sheet after laser processing.

To quantify the surface roughness of the Nb_2AlC-Gr and NbO_x-Gr electrodes, optical micrographs were acquired using a confocal laser scanning microscope (CLSM). The topographical variations are presented in Fig. 4e and h collectively with the 2D micrographs (Fig. 4f and i) along with their 3D false colour mapping micrographs (Fig. 4g and j), where the colour variations reflect the difference in height profiles. The average surface roughness (S_q) of the electrodes was investigated utilizing height profile analysis, yielding values of ≈9.79 μm and ≈7.30 μm for the Nb_2AlC-Gr and NbO_x-Gr electrodes, respectively. These findings correlate with the SEM morphological studies, which indicate that the particle size reduction in NbO_x-Gr indeed reduces the surface roughness, causing the formation of a smoother electrode surface. Such surface modifications could potentially lead to boosting the electrochemical performance of the electrodes. STEM micrographs (Fig. S5 in ESI†) of NbO_x-Gr electrodes further confirm the presence of Nb nanoparticles on the graphene sheet.

2.3 Electrochemical characterization for nitrate reduction reaction

Firstly, the electrochemical active surface area (ECSA) of each electrode was evaluated, as the ECSA plays an important role in the electrochemical activity of the material. The ECSA values obtained for Gr, Nb_2AlC-Gr, and NbO_x-Gr as working electrodes are 0.03 cm^{-2}, 0.07 cm^{-2}, and 0.33 cm^{-2}, respectively. The detailed experimental procedures and calculations are provided in the ESI, Fig. S6a–f.† The two-fold increase in the ECSA after integrating the Nb_2AlC-MAX phase into the graphene network, followed by the additional increment due to the electrochemical etching, is beneficial for electrochemical performance.

The combination of simple laser treatment with electrochemical etching is responsible for the effective improvement

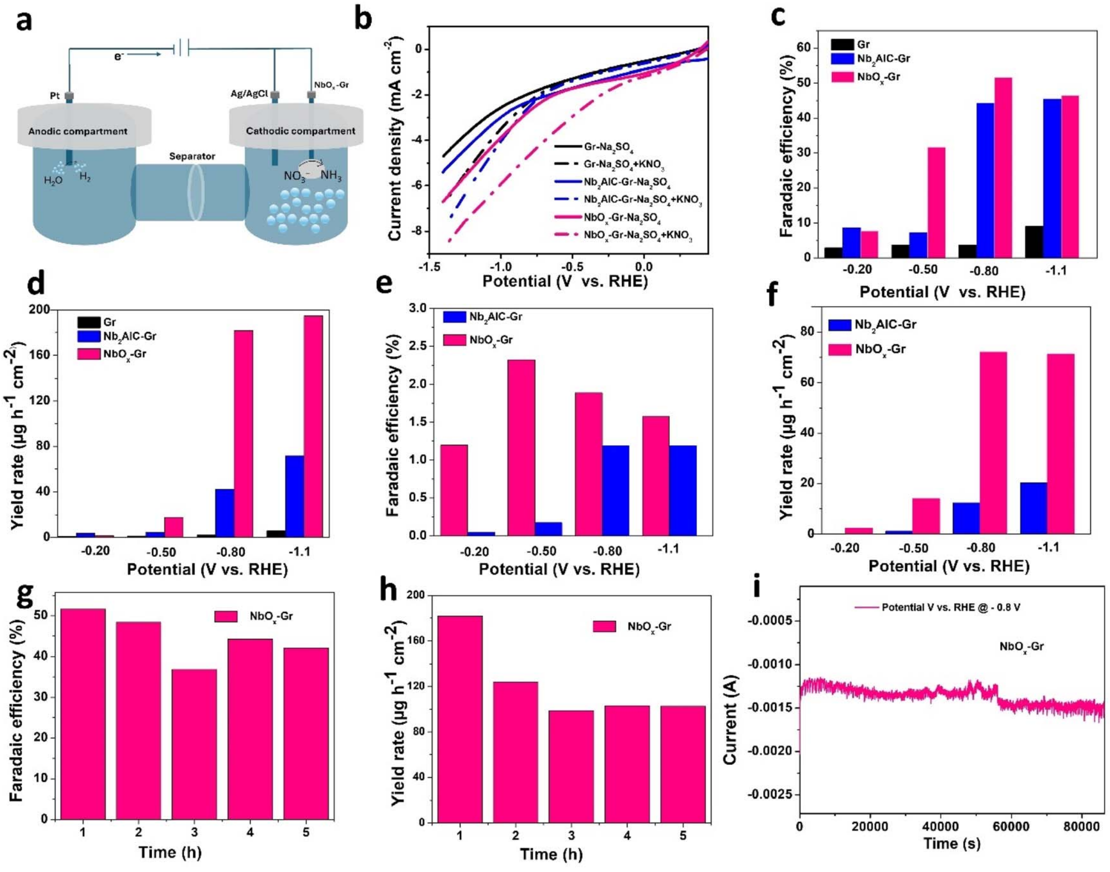

Fig. 5 Electrochemical characterization of the fabricated Gr, Nb_2AlC-Gr, and NbO_x-Gr electrodes: (a) three electrode set-up for nitrate reduction to ammonia. (b) Linear sweep voltammetry curve of Gr, Nb_2AlC-Gr, and NbO_x-Gr electrodes. (c and d) Faradaic efficiency and yield rate of Gr, Nb_2AlC-Gr, and NbO_x-Gr electrodes for ammonia detection at different potentials. (e and f) Faradaic efficiency and yield rate of Nb_2AlC-Gr, and NbO_x-Gr electrodes for nitrite detection at different potentials. (g and h) Ammonia generation measurement: faradaic efficiency and yield rate of the NbO_x-Gr electrode at different times. (i) Long-term stability measurement of the NbO_x-Gr electrode for 24 hours.

of ECSA of the NbO_x-Gr sample. Furthermore, the electrochemical activity of the electrocatalyst material for nitrate reduction to generate NH_3 and by-product NO_2^- ions is evaluated employing a three-electrode setup in an H-type glass cell, separated *via* a frit in an ambient environment, as shown in Fig. 5a. The Gr, Nb_2AlC-Gr, and NbO_x-Gr pendulum-shaped electrodes were employed as the working electrodes as illustrated in ESI Fig. S7,† where Pt acted as the counter electrode and Ag/AgCl acted as the reference electrode.

First, the linear sweep voltammetry (LSV) curve was recorded for Gr, Nb_2AlC-Gr and NbO_x-Gr as working electrodes in the absence of NO_3^- ions (0.5 M Na_2SO_4 electrolyte) and the presence of NO_3^- ions (0.5 M Na_2SO_4 + 0.1 M KNO_3 electrolyte) at a scan rate of 5 mV^{-1} as depicted in Fig. 5b. The LSV curves demonstrate that the Gr, Nb_2AlC-Gr, and NbO_x-Gr electrodes exhibit electrochemical activity for nitrate reduction as proven by the increment in the current density, in the presence of NO_3^- ions. The comparative LSV study further indicates that the NbO_x-Gr as a working electrode is the most efficient for nitrate reduction reaction, demonstrating the highest increment in the current density among all the tested electrodes. This enhanced electrochemical performance towards the nitrate reduction reaction of NbO_x-Gr aligns with the physical characterization findings, suggesting that the fabrication process involving laser treatment and *in situ* electrochemical etching of Al metal improves the electrochemical activity of the material.

To further confirm the electrochemical activity of Gr, Nb_2AlC-Gr, and NbO_x-Gr electrodes for nitrate reduction reaction, electrolysis was performed at selected potentials in the range of −0.20 to −1.10 V *vs.* RHE for 1-hour time duration, as illustrated in ESI Fig. S8a–c.† The electrolysis findings demonstrate an increase in the current density for the NbO_x-Gr electrode compared to the Gr and Nb_2AlC-Gr electrodes, aligning with the findings of LSV measurements. Next, the NH_3 concentration in the electrolytic solutions was quantified by employing the well-known indophenol blue colorimetric approach. The electrolytic solution upon the reaction with the indophenol blue reagent changes its colour from yellow to dark green, suggesting the formation of higher concentration of NH_3 for the electrolytic solution of the NbO_x-Gr electrode sample as depicted in ESI Fig. S9.† This indicates that ammonia is generated in high concentration when the potential is increased. The UV-vis spectra were recorded as shown in ESI Fig. S10a–c,† displaying an increase in peak intensity at 655 nm, which corresponds to ammonia detection.

The UV-vis spectra reveal a progressive increase in the ammonia peak as the potential is increased for the Gr, Nb_2AlC-Gr, and NbO_x-Gr electrodes. The NbO_x-Gr electrode shows the most efficient results for NH_3 generation compared to Gr and Nb_2AlC-Gr electrodes, corroborating with the results of LSV and electrochemical measurements. The faradaic efficiency (FE) and ammonia yield rate were calculated, utilizing the ammonia concentration acquired from the indophenol colorimetric approach utilizing eqn (1) and (2), illustrating a gradual enhancement when the potential is increased from −0.20 V to −1.1 V, as demonstrated in Fig. 5c and d. At −1.1 V *vs.* RHE, the FE and yield rates are ≈9.05% and ≈5.68 $\mu g\ h^{-1}\ cm^{-2}$ for the Gr electrode, ≈45.47% and ≈71.50 $\mu g\ h^{-1}\ cm^{-2}$ for the Nb_2AlC-Gr electrode, and ≈46.50% and ≈194.79 $\mu g\ h^{-1}\ cm^{-2}$ for the NbO_x-Gr electrode, respectively. The obtained yield rate is comparable with those of the previously reported MXene-based electrocatalysts for nitrate reduction to ammonia. The comparative table is provided in ESI Table S1.†

In addition to ammonia generation, nitrite ions are a primary by-product formed during the nitrate reduction reaction electrolysis process. Thus, to evaluate NO_2^- ions in the electrolytic solution, UV spectra were recorded for Nb_2AlC-Gr and NbO_x-Gr electrodes, as shown in ESI Fig. S11a and b.† The observed peaks at 540 nm indicate the presence of NO_2^- ions. Consequently, FE and yield rate were calculated utilizing the nitrite ion concentration, using eqn (1) and (2) as demonstrated in Fig. 5e and f. The FE and the yield rate of NO_2^- ions are lower compared to those of NH_3, which confirms that the electrocatalyst materials generate NO_2^- ions as a by-product. Furthermore, a potential of −0.8 V is selected for the stability measurements of the NbO_x-Gr electrode. The chronoamperometry measurement and UV spectra measurement are shown in ESI in Fig. S12 and 13,† confirms the formation of NH_3 at different times, as presented in Fig. 5g and h. Long-time electrolysis at a potential of −0.8 V was performed, which suggests that the NbO_x-Gr electrode was able to generate ammonia for 24 hours as demonstrated in Fig. 5i. Furthermore, the UV spectra (Fig. S14†) confirm the presence of an ammonia peak at 655 nm, with a calculated ammonia yield rate of 194.04 $\mu g\ h^{-1}\ cm^{-2}$. Moreover, to validate the conversion of NO_3^- ions into NH_3 through electrolysis, we acquired the ^1H NMR spectra of the electrolysis solution of the NbO_x-Gr electrode in a^{15}N-labeled NO_3 + 0.5 M Na_2SO_4 electrolyte and a blank electrolyte containing 0.5 M Na_2SO_4. The obtained spectra demonstrate that the blank solution has no signal (Fig. S15†), while in the ^{15}N-labeled NO_3 + 0.5 M Na_2SO_4 electrolytic solution we observed a 1 : 1 doublet and a 1 : 1 : 1 triplet peak, which could be related to NH_4^+ and its by-product.[61] Furthermore to confirm the presence of requisite elements on the surface and structural stability of NbO_x-Gr electrodes, SEM-EDS mapping micrographs were acquired before and after electrochemical analysis, which confirm the presence of elements like C, O, Nb, and Al on the surface of electrodes after electrochemical analysis, suggesting that the electrodes are stable as illustrated in Fig. S16 in the ESI.†

2.4 Theoretical calculations

Density functional theory (DFT) calculations were employed to investigate the mechanism of electrocatalytic conversion of NO_3^- to NH_3 over NbO_x-Gr. A model comprising a NbO_x nanocluster supported on pristine graphene was used to examine the structural reorganization of NbO_x upon adsorption on the graphene surface, construct the Gibbs free energy profile, and analyze charge density differences (CDD) and Bader charges.

Our calculations revealed a negative binding energy of −2.99 eV, indicating thermodynamically favorable adsorption of the NbO_x nanocluster on graphene (see details in the ESI†). Additionally, a geometry analysis showed that the NbO_x model underwent no substantial structural reorganization after adsorption on the graphene surface (Fig. S17†). The most

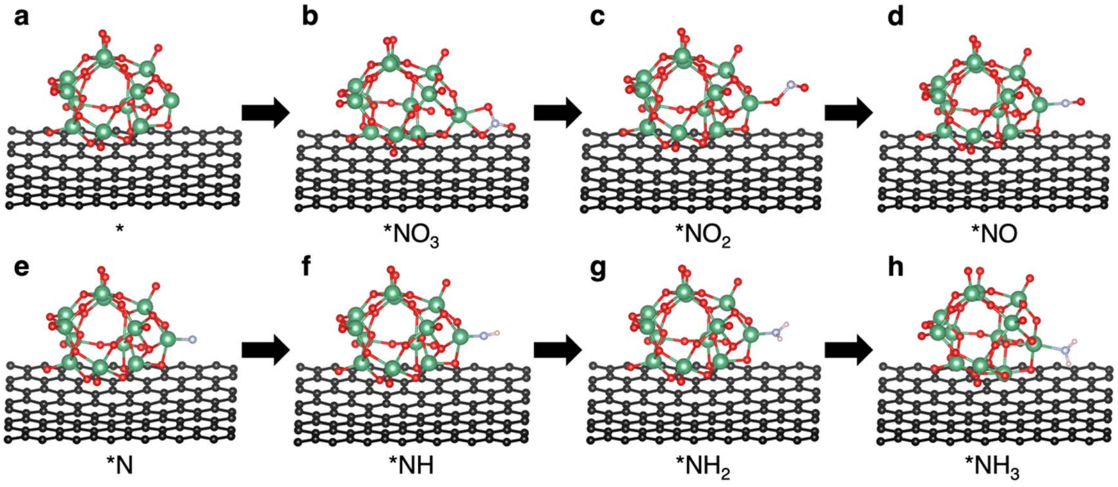

Fig. 6 (a–h) DFT optimized structures of the reaction intermediates for nitrate reduction over NbO_x-Gr.

pronounced deviation was observed for the O16 atom (Table S2†), attributed to the interaction of the Nb2 atom with the graphene sheet (see Fig. S17† for atom labelling). The observed changes correspond to those occurring upon non-covalent interaction between nanoclusters and graphene. Furthermore, the optimized structure of the NbO_x-Gr catalyst confirmed the absence of a covalent bond between the NbO_x nanocluster and the graphene support (Fig. 6a).

The Gibbs free energy profile displays the energy changes during nitrate reduction, which involves nine proton and eight electron transfers, following the sequence:[62] $NO_3^- \rightarrow *NO_3 \rightarrow *NO_2 \rightarrow *NO \rightarrow *N \rightarrow *NH \rightarrow *NH_2 \rightarrow *NH_3 \rightarrow NH_3(g)$ (Fig. 6).

Furthermore, DFT-optimized structures of the reaction intermediates identified the Nb atom on the NbO_x cluster surface as the active site. The reaction starts with the favourable

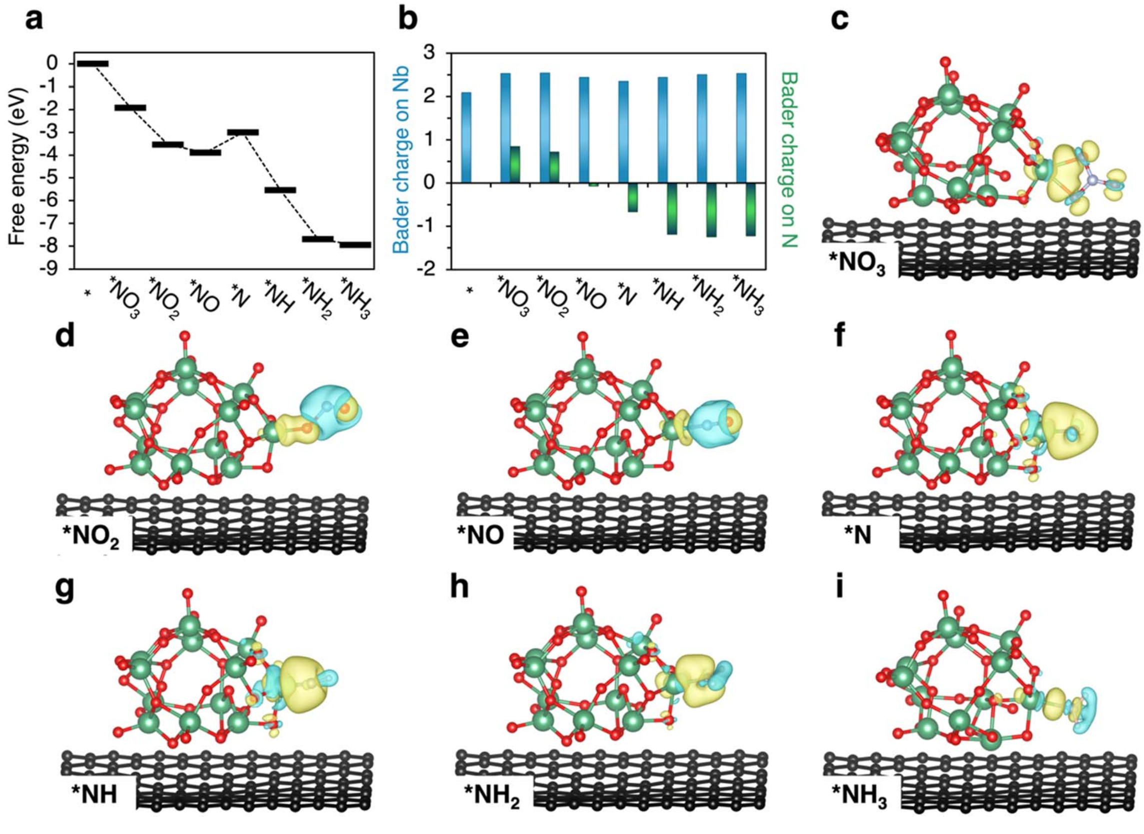

Fig. 7 (a) Gibbs free energy diagram of nitrate reduction ($U = 0$ V) catalysed by the model of NbO_x-Gr. (b) Bader charge of Nb atom (blue), which is the active site of the nitrate reduction intermediates, and N atom (green). (c–i) DFT calculated charge density difference (CDD) of the intermediate structures of nitrate to ammonia reduction. Yellow and blue display charge accumulation and depletion, respectively.

adsorption of the NO_3^- anion, which is strongly bound, exhibiting a Gibbs free change (ΔG) of -1.91 eV for this reaction step. Furthermore, Gibbs free energy changes were negative for all examined reaction steps along the reduction pathway, except for the *NO → *N step, which may serve as the potential-determining step (PDS). As depicted in Fig. 7a, the ΔG for this step is 0.88 eV. The corresponding limiting potential (U_L) of -0.44 V for the overall energy profile suggests that NbO_x-Gr can act as an effective electrocatalyst for nitrate reduction.

The electronic structure of the intermediates was further probed, and the calculated CDDs revealed distinct charge accumulation patterns. For oxygen-containing intermediates ($*NO_3$, $*NO_2$, and *NO), charge accumulation primarily occurs on bonds connecting the active site (Nb atom) and oxygen atoms (Fig. 7c–e). In contrast, a high accumulation of charge on the N atom was observed for the *N intermediate (Fig. 7). This can explain the strongly negative ΔG of -2.53 eV associated with the *N → *NH reaction step. Similar charge accumulation on the nitrogen atoms was found for $*NH_2$ and $*NH_3$ intermediates (Fig. 7h–i). The facile hydrogenation steps in nitrate reduction on NbO_x-Gr can also be inferred from Bader charge analysis, which reveals an increasing negative charge on nitrogen atoms as the reaction progresses (Fig. 7b).

3 Conclusion

In summary, we reported a new kind of electrode material for nitrate reduction to ammonia, which was fabricated by employing a single-step lasing process followed by the electrochemical etching technique. The lasing process concurrently modified the chemical composition of the Nb_2AlC phase and converted the polyimide substrate into a graphene structure. Moreover, the *in situ* electrochemical etching technique etched the aluminium metal from the surface of the electrocatalyst electrode, enhancing its electrochemical activity. This fabricated heterostructure of NbO_x-Gr electrode delivered a faradaic efficiency and ammonia yield rate of $\approx 46.50\%$ and ≈ 194.79 μg h^{-1} cm^{-2}, respectively, at -1.1 V *vs.* RHE. Additionally, theoretical calculations provided a deeper understanding of the reaction mechanism of the nitrate reduction to NH_3, confirming that the electrochemical active site is present on the Nb atom of the NbO_x-Gr electrode. In the future direction, the present work exhibits huge potential for the fabrication of cost-effective Nb_2AlC electrocatalyst materials for nitrate reduction to ammonia, offering an advanced material fabrication strategy to achieve high faradaic efficiency and yield rate for ammonia generation through the introduction of suitable MAX phases.

4 Materials and experimental methods

4.1 Materials

Nb_2AlC powder was obtained from Laizhou Kai Ceramic Materials Co., Ltd, China. Polyimide sheets (PI, 0.005″) were used as received from Fiedler Scientific Instruments, Czech Republic. Hydrochloric acid (35%) was obtained from Penta Chemicals Unlimited. Potassium nitrate was procured from Alfa Aesar. Sodium hypochlorite solution, phosphoric acid, salicylic acid, sodium hydroxide, citric acid, sodium nitroferricyanide, *N*-(1-naphthyl) ethylenediamine dihydrochloride, sulfanilamide, $Na^{15}NO_3$ and sodium sulfate were acquired from Merck. All the chemicals were used as procured and all the solutions were prepared using Millipore water with a resistivity of >18 MΩ cm.

4.2 Laser treatment of Nb_2AlC-Gr electrodes

The Gr, Nb_2AlC-Gr, and NbO_x-Gr electrodes were fabricated using a Laser dicer Oxford Lasers A-Series equipped with a diode-pumped solid-state Nd:YAG laser operating at 532 nm wavelength. The defocused laser writing technique was directly applied on polyimide sheets to fabricate the Gr electrode. In contrast, for the Nb_2AlC-Gr electrode, firstly, Nb_2AlC dispersed in ethanol was drop-cast onto the polyimide sheets before defocused laser writing. The laser parameters used in this study were as follows: a pulse frequency of 7 kHz, a scanning speed of 50 mm s^{-1}, and a laser power of 3 W.

4.3 *In situ* electrochemical etching

A three-electrode set-up, where Ag/AgCl acts as the reference electrode, Platinum (Pt) acts as the counter electrode, and Nb_2AlC-Gr acts as the working electrode, was employed for the electrochemical etching process. A potential of 2 V *vs.* Ag/AgCl was applied for the chronoamperometry measurement in 3 M HCl as the electrolyte. The etching process was performed for different time durations like 6 h, 12 h, 18 h, and 24 h under room temperature conditions. After the etching the electrodes were rinsed with H_2O, to remove any residual impurity and $AlCl_3$ on the surface of the electrodes.

4.4 Electrochemical measurement

All the electrochemical experiments were carried out employing a three-electrode setup. The linear sweep voltammetry profile was obtained in 0.5 M Na_2SO_4 and 0.5 M Na_2SO_4 + 0.1 M KNO_3 (nitrate source) electrolyte with the scan rate of 5 mV^{-1} using a potentiostat instrument (PGSTAT 204 from Metrohm Autolab, Netherlands) that was operated through NOVA software version 2.1, connected with a computer. The chronoamperometry measurements were carried out using 0.5 M Na_2SO_4 + 0.1 M KNO_3 (nitrate source) as the electrolyte, a Ag/AgCl electrode filled with the KCl gel electrolyte as the reference electrode, Platinum (Pt) as the counter electrode, and Gr, Nb_2AlC-Gr, and NbO_x-Gr as the working electrode in a similar setup.

To investigate the nitrate reduction reaction activity. The electrolysis process to generate ammonia was conducted in an H-cell separated *via* a frit. To ensure a balanced distribution of electrolytes, 20 mL of electrolyte was added to both the anodic and cathodic compartments. The electrolysis process was carried out for one hour for each electrode like Gr, Nb_2AlC-Gr, and NbO_x-Gr with continuous stirring to investigate the faradaic efficiency (FE%) and the ammonia yield rate. During the electrolysis process, different potentials were applied in the range of -0.20 to -1.10 V *vs.* RHE. The potential was converted into a reversible hydrogen electrode (RHE) scale using the following equation: $E_{\mathrm{RHE}} = E_{\mathrm{Ag/AgCl}} + 0.0591\ \mathrm{pH} + 0.199$.[63]

4.5 Colorimetric procedure for the quantification of NH_3 and NO_2^- concentrations

A well-established colorimetric analysis procedure was employed to evaluate the NH_3 and NO_2^- ion concentration after the electrolytic measurements. A UV-vis spectrophotometer was employed to identify the concentration of NH_3 and NO_2^- ions. The detailed procedure is described in subsequent sections.

4.5.1 Quantification of ammonia (NH_3). The quantification of ammonia is carried out using the electrolytic solution obtained after the chronoamperometry analysis employing a UV-visible spectrophotometer (JASCO V-750). To quantify the presence of the generated ammonia in the electrolytic solution, a certain volume of the solution was taken out from the H-cell and diluted up to 600 μL to reach the detection limit, followed by the addition of 600 μL of a solution comprising 3 M NaOH, 10 wt% salicylic acids, and 10 wt% citric acid, 300 μL of a solution consisting of 0.2 M NaClO, and 60 μL of a solution containing 2.0 wt% sodium nitroferricyanide. This mixture was kept for two hours. The UV-vis absorbance spectrum was acquired. The ammonia concentration was estimated on the formation of the indophenol blue product in the above mixture and the absorbance spectrum was recorded at 655 nm wavelength. Additionally, the ammonia concentration was calculated using the equation $y = 0.0079 \times -0.0071$, $R^2 = 0.999$, utilizing a calibration curve derived from a series of standard ammonium chloride solutions in the 0.5 M Na_2SO_4 electrolyte.[63]

4.5.2 Quantification of nitrite (NO_2^-). The nitrite concentration in the electrolytic solution was determined following a reported protocol, where a colouring reagent was formulated by adding *N*-(1-naphthyl) ethylenediamine dihydrochloride (0.02 g) and *p*-amino benzenesulfonamide (0.4 g) in water (5 mL) along with phosphoric acid (1 mL, $\rho = 1.70$ g mL^{-1}). Later, a specified amount of the electrolytic solution was taken out and diluted to 1.5 mL to meet the detection range. Subsequently, 50 μL of colour reagent was mixed in the above diluted electrolytic solution. The mixture of the solution was kept for 20 minutes. Then, the UV-visible absorption spectra were acquired. The nitrite concentration was investigated by recording the peak intensity at 540 nm wavelength and the concentration is calculated using the calibration curve.[63]

4.6 Calculation to determine the performance of the working electrodes (electrocatalysts)

The faradaic efficiency (FE) and yield rate (YR) were obtained by the following equations:[63]

$$\mathrm{FE}\ (\%) = (n \times F \times c_{\mathrm{NH_3/NO_2^-}} \times V)/Q \tag{1}$$

$$\mathrm{YR} = (c_{\mathrm{NH_3/NO_2^-}} \times V \times M)/(t \times A) \tag{2}$$

where n is the number of electrons (8 for NH_3 and 2 for NO_2^-), F represents the faradaic constant (96 485 C mol^{-1}), $c_{\mathrm{NH_3/NO_2^-}}$ is the concentration of NH_3 or NO_2^-, V is the electrolytic solution volume (20 mL) at the cathodic compartment, Q is the total charge observed during the process of electrolysis, M is 17.03 for NH_3 or 46.005 for NO_2^-, t is the electrolysis time, and A is the surface area of the working electrode.

4.7 Evaluation of ammonia by the ^{1}H NMR quantitative technique and isotopic labelling measurement

For the isotopic labelling analysis, the electrolysis was recorded in the 0.5 M Na_2SO_4 + 0.1 M $Na^{15}NO_3$ electrolyte solution. Following electrolysis, an aliquot of 5 mL catholyte was collected from the H-cell and 250 μL of concentrated H_2SO_4 was added to create an acidic environment, which is the standard for the quantification of NH_4^+ ions. After this, 0.002 g of maleic acid was added as an internal standard to the above solution. 500 μL of this solution was taken in the NMR tube and 50 μL deuterium oxide (D_2O) was added for the NMR detection.[63]

4.8 Material characterization

SEM (FEI VERIOS 460 L) is used for the surface morphology investigation of the Gr, Nb_2AlC-Gr, and NbO_x-Gr electrodes. An Olympus Lext-OLS4100 confocal laser scanning microscope is utilized to obtain the optical images of the Nb_2AlC-Gr and NbO_x-Gr electrodes. Physical characterization of Nb_2AlC-Gr and NbO_x-Gr electrodes was performed using a Rigaku SmartLab 3 kW X-ray diffractometer for the X-ray diffraction (XRD) investigation. This XRD device was operated with a current of 30 mA and a voltage of 40 kV. The XRD investigation was carried out following the Bragg Brentano geometry with Cu Kα radiation ($\lambda = 0.15418$ nm). The chemical composition investigation was carried out using an X-ray photoelectron spectroscopy device (XPS, Kratos AXIS Supra). The XPS wide survey scan and core level spectra of the elements like Nb, C, O, and Al present in Gr, commercial Nb_2AlC, Nb_2AlC-Gr, and NbO_x-Gr are acquired. The software Casa XPS is employed for the fitting of XPS spectra curves, and the calibration of the obtained spectra is done against the carbon C 1s peak *i.e.*, 284.8 eV. A Witec Alpha 300R instrument is utilized to obtain the Raman spectra curve. The UV-visible absorption spectra studies are performed with a UV-Vis-spectrophotometer JASCO V-750.

4.9 Theoretical calculations

Spin-polarized DFT calculations were carried out using the Vienna *Ab initio* Simulation Package (VASP), introducing the projector augmented wave (PAW) potentials with a plane-wave cutoff energy of 520 eV.[64–67] The Perdew–Burke–Ernzerhof (PBE) parametrization of the generalized gradient approximation (GGA) was used to describe the electronic exchange–correlation energies, and the DFT-D3 method of Grimme with zero-damping was also introduced to describe the van der Waals interactions.[68,69] All structures were fully optimized until forces acting on all atoms were reduced to 0.03 eV Å^{-1}, and electronic degrees of freedom were relaxed until the change in total electronic energy between successive iteration steps was smaller than 10^{-5} eV. For structural optimization, the Brillouin zone was sampled using a $1 \times 1 \times 1$ *k*-point grid based on the Monkhorst–Pack scheme, centred at Gamma. Since the nitrate reduction proceeds in an aqueous environment and involves H^+ transfer, the solvation effects of water were considered by VASPsol.[70] To eliminate the effects between two adjacent layers, a vacuum region of 15 Å was added in the *z*-direction. For electronic structure calculations, the Brillouin zone integrations were performed with a gamma-centred 3 × 3 × 1 Monkhorst–Pack *k*-point mesh grid.[71] The computational hydrogen electrode (CHE) model was used to calculate the Gibbs free energy of reactions involving electron-proton transfer. The vibrational modes were calculated at 298.15 K to obtain the zero-point energy, entropy, and temperature corrections to enthalpy, and VASPKIT was used for the post-processing.[72,73] To avoid calculating the charged molecule NO_3^-, the Gibbs free energy of aqueous NO_3^- was derived from those of gaseous HNO_3 and H_2. The Gibbs free energy for nitrate NO_3^- to adsorb on the NbO_x-Gr model in aqueous solution forming $*NO_3$ was calculated as follows:[74,75]

$$\Delta G_{*NO_3} = G_{*NO_3} - G_{*} - G_{*HNO_3(g)} + \frac{1}{2}G_{H_2(g)} + 0.392,$$

where G_{*NO_3}, G_{*}, $G_{*HNO_3(g)}$, and $G_{H_2(g)}$ are the Gibbs free energies of NO_3^- adsorbed on the NbO_x-Gr model, the NbO_x-Gr model itself, HNO_3 and H_2 molecules in the gas phase, respectively. The value of 0.392 is the correction of adsorption energy.[76] Limiting potential U_L ($U_L = -\Delta G_{max}/e$) was employed to describe the lowest bias requirement for the nitrate reduction.[77]

Data availability

Data for this article are available at ZENODO at **https://zenodo.org**.

Author contributions

S. N., S. D., and M. P. conceived the idea. S. N. carried out laser treatment, *in situ* etching of the Nb_2AlC electrodes and their characterizations (such as SEM, CLSM, XPS, XRD, Raman, electrochemical characterization, and ammonia production), data acquisition, investigation and preparation of the first draft of the manuscript. S. D. carried out laser treatment, managed the project, and revised the manuscript. M. L. performed theoretical calculations and wrote the theoretical section. M. O. participated in the validation of the theoretical calculations, writing of the manuscript and funding acquisition. M. P. supervised the research, acquired funding, and revised the manuscript. All the data included in the manuscript were discussed and approved by all the authors.

Conflicts of interest

The authors affirm no conflict of financial interest.

Acknowledgements

S. N. would like to acknowledge Mendelu PhD talent award for funding and Josef Dadok National NMR Centre, CEITEC, Central European Institute of technology, Masaryk University for NMR measurements. The work was supported by the ERDF/ESF project TECHSCALE (No. CZ.02.01.01/00/22_008/0004587). The material characterization was done with the support of the CzechNanoLab project at CEITEC Nano Research Infrastructure MEYS CR (LM2023051). M. L. acknowledges VSB – Technical University of Ostrava, IT4Innovations National Supercomputing Center, Czech Republic, for awarding this project access to the LUMI supercomputer, owned by the EuroHPC Joint Undertaking, hosted by CSC (Finland) and the LUMI consortium through the Ministry of Education, Youth and Sports of the Czech Republic through the e-INFRA CZ (grant ID: 90254). M. P., M. L. and M. O. acknowledge that this research was co-funded by the European Union under the REFRESH-Research Excellence For Region Sustainability and High-tech Industries project number CZ.10.03.01/00/22_003/0000048 *via* the Operational Programme Just Transition.

References

1 M. Duca and M. T. M. Koper, Powering Denitrification: The Perspectives of Electrocatalytic Nitrate Reduction, *Energy Environ. Sci.*, 2012, **5**(12), 9726, DOI: **10.1039/c2ee23062c**.

2 P. H. van Langevelde, I. Katsounaros and M. T. M. Koper, Electrocatalytic Nitrate Reduction for Sustainable Ammonia Production, *Joule*, 2021, **5**(2), 290–294, DOI: **10.1016/j.joule.2020.12.025**.

3 L. Li, C. Tang, D. Yao, Y. Zheng and S.-Z. Qiao, Electrochemical Nitrogen Reduction: Identification and Elimination of Contamination in Electrolyte, *ACS Energy Lett.*, 2019, **4**(9), 2111–2116, DOI: **10.1021/acsenergylett.9b01573**.

4 S. Li, X. Fu, J. K. Nørskov and I. Chorkendorff, Towards Sustainable Metal-Mediated Ammonia Electrosynthesis, *Nat. Energy*, 2024, **9**(11), 1344–1349, DOI: **10.1038/s41560-024-01622-7**.

5 S. Ye, Z. Chen, G. Zhang, W. Chen, C. Peng, X. Yang, L. Zheng, Y. Li, X. Ren, H. Cao, D. Xue, J. Qiu, Q. Zhang and J. Liu, Elucidating the Activity, Mechanism and Application of Selective Electrosynthesis of Ammonia from Nitrate on Cobalt Phosphide, *Energy Environ. Sci.*, 2022, **15**(2), 760–770, DOI: **10.1039/D1EE03097C**.

6 J. Wang, T. Feng, J. Chen, V. Ramalingam, Z. Li, D. M. Kabtamu, J.-H. He and X. Fang, Electrocatalytic Nitrate/Nitrite Reduction to Ammonia Synthesis Using Metal Nanocatalysts and Bio-Inspired Metalloenzymes, *Nano Energy*, 2021, **86**, 106088, DOI: **10.1016/j.nanoen.2021.106088**.

7 F. Haber and R. Le Rossignol, Über Die Technische Darstellung von Ammoniak Aus Den Elementen, *Z. Elektrochem. Angew. Phys. Chem.*, 1913, **19**(2), 53–72, DOI: **10.1002/bbpc.19130190201**.

8 T. Kandemir, M. E. Schuster, A. Senyshyn, M. Behrens and R. Schlögl, The Haber–Bosch Process Revisited: On the Real Structure and Stability of "Ammonia Iron" under Working Conditions, *Angew. Chem., Int. Ed.*, 2013, **52**(48), 12723–12726, DOI: **10.1002/anie.201305812**.

9 N. Hazari, Homogeneous Iron Complexes for the Conversion of Dinitrogen into Ammonia and Hydrazine, *Chem. Soc. Rev.*, 2010, **39**(11), 4044, DOI: **10.1039/b919680n**.

10 D. Ye and S. C. E. Tsang, Prospects and Challenges of Green Ammonia Synthesis, *Nat. Synth.*, 2023, **2**(7), 612–623, DOI: **10.1038/s44160-023-00321-7**.

11 J. W. Erisman, M. A. Sutton, J. Galloway, Z. Klimont and W. Winiwarter, How a Century of Ammonia Synthesis Changed the World, *Nat. Geosci.*, 2008, **1**(10), 636–639, DOI: **10.1038/ngeo325**.

12 G. Soloveichik, Electrochemical Synthesis of Ammonia as a Potential Alternative to the Haber–Bosch Process, *Nat. Catal.*, 2019, **2**(5), 377–380, DOI: **10.1038/s41929-019-0280-0**.

13 B. H. R. Suryanto, H.-L. Du, D. Wang, J. Chen, A. N. Simonov and D. R. MacFarlane, Challenges and Prospects in the Catalysis of Electroreduction of Nitrogen to Ammonia, *Nat. Catal.*, 2019, **2**(4), 290–296, DOI: **10.1038/s41929-019-0252-4**.

14 G. Qing, R. Ghazfar, S. T. Jackowski, F. Habibzadeh, M. M. Ashtiani, C.-P. Chen, M. R. Smith and T. W. Hamann, Recent Advances and Challenges of Electrocatalytic N_2 Reduction to Ammonia, *Chem. Rev.*, 2020, **120**(12), 5437–5516, DOI: **10.1021/acs.chemrev.9b00659**.

15 D. Hao, Z. Chen, M. Figiela, I. Stepniak, W. Wei and B.-J. Ni, Emerging Alternative for Artificial Ammonia Synthesis through Catalytic Nitrate Reduction, *J. Mater. Sci. Technol.*, 2021, **77**, 163–168, DOI: **10.1016/j.jmst.2020.10.056**.

16 Y. Wang, C. Wang, M. Li, Y. Yu and B. Zhang, Nitrate Electroreduction: Mechanism Insight, *in Situ* Characterization, Performance Evaluation, and Challenges, *Chem. Soc. Rev.*, 2021, **50**(12), 6720–6733, DOI: **10.1039/D1CS00116G**.

17 N. Hoang Truong, J.-S. Kim, J. Lim and H. Shin, Electrochemical Reduction of Nitrate to Ammonia: Recent Progress and Future Directions, *Chem. Eng. J.*, 2024, **495**, 153108, DOI: **10.1016/j.cej.2024.153108**.

18 J. Wan, H. Zhang, J. Yang, J. Zheng, Z. Han, W. Yuan, B. Lan and X. Li, Synergy between Fe and Mo Single Atom Catalysts for Ammonia Electrosynthesis, *Appl. Catal., B*, 2024, **347**, 123816, DOI: **10.1016/j.apcatb.2024.123816**.

19 Y. Ren, S. You, Y. Wang, J. Yang and Y. Liu, Bioinspired Tandem Electrode for Selective Electrocatalytic Synthesis of Ammonia from Aqueous Nitrate, *Environ. Sci. Technol.*, 2024, **58**(4), 2144–2152, DOI: **10.1021/acs.est.3c09759**.

20 G. Zhang, X. Li, K. Chen, Y. Guo, D. Ma and K. Chu, Tandem Electrocatalytic Nitrate Reduction to Ammonia on MBenes, *Angew. Chem., Int. Ed.*, 2023, **62**(13), e202300054, DOI: **10.1002/anie.202300054**.

21 Y. Xiong, Y. Wang, J. Zhou, F. Liu, F. Hao and Z. Fan, Electrochemical Nitrate Reduction: Ammonia Synthesis and the Beyond, *Adv. Mater.*, 2024, **36**(17), 2304021, DOI: **10.1002/adma.202304021**.

22 J. Lim, C.-Y. Liu, J. Park, Y.-H. Liu, T. P. Senftle, S. W. Lee and M. C. Hatzell, Structure Sensitivity of Pd Facets for Enhanced Electrochemical Nitrate Reduction to Ammonia, *ACS Catal.*, 2021, **11**(12), 7568–7577, DOI: **10.1021/acscatal.1c01413**.

23 D. Liu, L. Qiao, S. Peng, H. Bai, C. Liu, W. F. Ip, K. H. Lo, H. Liu, K. W. Ng, S. Wang, X. Yang and H. Pan, Recent Advances in Electrocatalysts for Efficient Nitrate Reduction to Ammonia, *Adv. Funct. Mater.*, 2023, **33**(43), 2303480, DOI: **10.1002/adfm.202303480**.

24 W. Chen, X. Yang, Z. Chen, Z. Ou, J. Hu, Y. Xu, Y. Li, X. Ren, S. Ye, J. Qiu, J. Liu and Q. Zhang, Emerging Applications, Developments, Prospects, and Challenges of Electrochemical Nitrate-to-Ammonia Conversion, *Adv. Funct. Mater.*, 2023, **33**(29), 2300512, DOI: **10.1002/adfm.202300512**.

25 I. M. u. Hasan, N. Xu, Y. Liu, M. Z. Nawaz, H. Feng and J. Qiao, Noble and Non-Noble Metal Based Catalysts for Electrochemical Nitrate Reduction to Ammonia: Activity, Selectivity and Stability, *Electrochem. Energy Rev.*, 2024, **7**(1), 36, DOI: **10.1007/s41918-024-00236-7**.

26 Z.-L. Xie, D. Wang and X.-Q. Gong, Theoretical Insights into Nitrate Reduction to Ammonia over Pt/TiO_2 : Reaction Mechanism, Activity Regulation, and Catalyst Design, *ACS Catal.*, 2022, **12**(16), 9887–9896, DOI: **10.1021/acscatal.2c01694**.

27 Y. Wang, W. Zhou, R. Jia, Y. Yu and B. Zhang, Unveiling the Activity Origin of a Copper-based Electrocatalyst for Selective Nitrate Reduction to Ammonia, *Angew. Chem., Int. Ed.*, 2020, **59**(13), 5350–5354, DOI: **10.1002/anie.201915992**.

28 F. Zhao, G. Hai, X. Li, Z. Jiang and H. Wang, Enhanced Electrocatalytic Nitrate Reduction to Ammonia on Cobalt Oxide Nanosheets via Multiscale Defect Modulation, *Chem. Eng. J.*, 2023, **461**, 141960, DOI: **10.1016/j.cej.2023.141960**.

29 J. Choi, S. Im, J. Choi, S. Surendran, D. J. Moon, J. Y. Kim, J. K. Kim and U. Sim, Recent Advances in 2D Structured Materials with Defect-Exploiting Design Strategies for Electrocatalysis of Nitrate to Ammonia, *Energy Mater.*, 2024, **4**(2), 400020, DOI: **10.20517/energymater.2023.67**.

30 X. Zhang, Y. Wang, C. Liu, Y. Yu, S. Lu and B. Zhang, Recent Advances in Non-Noble Metal Electrocatalysts for Nitrate Reduction, *Chem. Eng. J.*, 2021, **403**, 126269, DOI: **10.1016/j.cej.2020.126269**.

31 H. Zhang, H. Wang, X. Cao, M. Chen, Y. Liu, Y. Zhou, M. Huang, L. Xia, Y. Wang, T. Li, D. Zheng, Y. Luo, S. Sun, X. Zhao and X. Sun, Unveiling Cutting-Edge Developments in Electrocatalytic Nitrate-to-Ammonia Conversion, *Adv. Mater.*, 2024, **36**(16), 2312746, DOI: **10.1002/adma.202312746**.

32 H. Xu, Y. Ma, J. Chen, W. Zhang and J. Yang, Electrocatalytic Reduction of Nitrate – a Step towards a Sustainable Nitrogen Cycle, *Chem. Soc. Rev.*, 2022, **51**(7), 2710–2758, DOI: **10.1039/D1CS00857A**.

33 M. Sokol, V. Natu, S. Kota and M. W. Barsoum, On the Chemical Diversity of the MAX Phases, *Trends Chem.*, 2019, **1**(2), 210–223, DOI: **10.1016/j.trechm.2019.02.016**.

34 Md. S. Alam, M. A. Chowdhury, T. Khandaker, M. S. Hossain, M. S. Islam, M. M. Islam and M. K. Hasan, Advancements in MAX Phase Materials: Structure, Properties, and Novel Applications, *RSC Adv.*, 2024, **14**(37), 26995–27041, DOI: **10.1039/D4RA03714F**.

35 K. R. G. Lim, M. Shekhirev, B. C. Wyatt, B. Anasori, Y. Gogotsi and Z. W. Seh, Fundamentals of MXene Synthesis, *Nat. Synth.*, 2022, **1**(8), 601–614, DOI: **10.1038/s44160-022-00104-6**.

36 S. Kumar, Fluorine-Free MXenes: Recent Advances, Synthesis Strategies, and Mechanisms, *Small*, 2024, **20**(16), 2308225, DOI: **10.1002/smll.202308225**.

37 S. Nouseen, S. Deshmukh and M. Pumera, Nanoarchitectonics of Laser Induced MAX 3D-Printed Electrode for Photo-Electrocatalysis and Energy Storage Application with Long Cyclic Durability of 100 000 Cycles, *Adv. Funct. Mater.*, 2024, **34**(45), 2407071, DOI: **10.1002/adfm.202407071**.

38 Z. M. Sun, Progress in Research and Development on MAX Phases: A Family of Layered Ternary Compounds, *Int. Mater. Rev.*, 2011, **56**(3), 143–166, DOI: **10.1179/1743280410Y.0000000001**.

39 S. Huang, Z. Wang, Y. Von Lim, Y. Wang, Y. Li, D. Zhang and H. Y. Yang, Recent Advances in Heterostructure Engineering for Lithium–Sulfur Batteries, *Adv. Energy Mater.*, 2021, **11**(10), 2003689, DOI: **10.1002/aenm.202003689**.

40 P. Wang, K. Jiang, G. Wang, J. Yao and X. Huang, Phase and Interface Engineering of Platinum–Nickel Nanowires for Efficient Electrochemical Hydrogen Evolution, *Angew. Chem.*, 2016, **128**(41), 13051–13055, DOI: **10.1002/ange.201606290**.

41 J. Lv, X. Sun, F. Wang, R. Yang, T. Zhang, T. Liang, W. Rong, Q. Yang, W. Xue, L. Wang, X. Xu and Y. Liu, Engineering Nickel Dopants in Atomically Thin Molybdenum Disulfide for Highly Efficient Nitrate Reduction to Ammonia, *Adv. Funct. Mater.*, 2024, **34**(49), 2411491, DOI: **10.1002/adfm.202411491**.

42 J. Lin, Z. Peng, Y. Liu, F. Ruiz-Zepeda, R. Ye, E. L. G. Samuel, M. J. Yacaman, B. I. Yakobson and J. M. Tour, Laser-Induced Porous Graphene Films from Commercial Polymers, *Nat. Commun.*, 2014, **5**(1), 5714, DOI: **10.1038/ncomms6714**.

43 L. X. Duy, Z. Peng, Y. Li, J. Zhang, Y. Ji and J. M. Tour, Laser-Induced Graphene Fibers, *Carbon*, 2018, **126**, 472–479, DOI: **10.1016/j.carbon.2017.10.036**.

44 R. Ye, D. K. James and J. M. Tour, Laser-Induced Graphene: From Discovery to Translation, *Adv. Mater.*, 2019, **31**(1), 1803621, DOI: **10.1002/adma.201803621**.

45 R. Ye, D. K. James and J. M. Tour, Laser-Induced Graphene, *Acc. Chem. Res.*, 2018, **51**(7), 1609–1620, DOI: **10.1021/acs.accounts.8b00084**.

46 J. Chen, M. Chen, W. Zhou, X. Xu, B. Liu, W. Zhang and C. Wong, Simplified Synthesis of Fluoride-Free $Ti_3C_2T_x$ via Electrochemical Etching toward High-Performance Electrochemical Capacitors, *ACS Nano*, 2022, **16**(2), 2461–2470, DOI: **10.1021/acsnano.1c09004**.

47 C. Wang, H. Shou, S. Chen, S. Wei, Y. Lin, P. Zhang, Z. Liu, K. Zhu, X. Guo, X. Wu, P. M. Ajayan and L. Song, HCl-Based Hydrothermal Etching Strategy toward Fluoride-Free MXenes, *Adv. Mater.*, 2021, **33**(27), 2101015, DOI: **10.1002/adma.202101015**.

48 Z. U. Din Babar, J. Fatheema, N. Arif, M. S. Anwar, S. Gul, M. Iqbal and S. Rizwan, Magnetic Phase Transition from Paramagnetic in Nb_2 AlC-MAX to Superconductivity-like Diamagnetic in Nb_2 C-MXene: An Experimental and Computational Analysis, *RSC Adv.*, 2020, **10**(43), 25669–25678, DOI: **10.1039/D0RA04568C**.

49 B. Sindhu, A. Kothuru, P. Sahatiya, S. Goel and S. Nandi, Laser-Induced Graphene Printed Wearable Flexible Antenna-Based Strain Sensor for Wireless Human Motion Monitoring, *IEEE Trans. Electron Devices*, 2021, **68**(7), 3189–3194, DOI: **10.1109/TED.2021.3067304**.

50 T. Li, G. Nam, K. Liu, J.-H. Wang, B. Zhao, Y. Ding, L. Soule, M. Avdeev, Z. Luo, W. Zhang, T. Yuan, P. Jing, M. G. Kim, Y. Song and M. Liu, A Niobium Oxide with a Shear Structure and Planar Defects for High-Power Lithium Ion Batteries, *Energy Environ. Sci.*, 2022, **15**(1), 254–264, DOI: **10.1039/D1EE02664J**.

51 L. Gao, H. Chen, F. Zhang, S. Mei, Y. Zhang, W. Bao, C. Ma, P. Yin, J. Guo, X. Jiang, S. Xu, W. Huang, X. Feng, F. Xu, S. Wei and H. Zhang, Ultrafast Relaxation Dynamics and Nonlinear Response of Few-Layer Niobium Carbide MXene, *Small Methods*, 2020, **4**(8), 2000250, DOI: **10.1002/smtd.202000250**.

52 H. Lin, S. Gao, C. Dai, Y. Chen and J. Shi, A Two-Dimensional Biodegradable Niobium Carbide (MXene) for Photothermal Tumor Eradication in NIR-I and NIR-II Biowindows, *J. Am. Chem. Soc.*, 2017, **139**(45), 16235–16247, DOI: **10.1021/jacs.7b07818**.

53 N. J. Lane, M. Naguib, V. Presser, G. Hug, L. Hultman and M. W. Barsoum, First-order Raman Scattering of the MAX Phases Ta_4AlC_3, Nb_4AlC_3, Ti_4AlN_3, and Ta_2AlC, *J. Raman Spectrosc.*, 2012, **43**(7), 954–958, DOI: **10.1002/jrs.3101**.

54 W. Li, D. Peng, W. Huang, X. Zhang, Z. Hou, W. Zhang, B. Lin and Z. Xing, Adjusting Coherence Length of Expanded Graphite by Self-Activation and Its Electrochemical Implication in Potassium Ion Battery, *Carbon*, 2023, **204**, 315–324, DOI: **10.1016/j.carbon.2022.12.072**.

55 J. Wang, S. Yang, C. Xiao, Z. Yu, R. Ren and X. Xiong, Effects of Atmospheric Pressure Plasma Treatment and Its Aging Behaviors on Interfacial Strength of PI/PEEK Composite Film, *J. Appl. Polym. Sci.*, 2025, **142**(3), e56369, DOI: **10.1002/app.56369**.

56 P. Arunkumar, A. G. Ashish, B. Babu, S. Sarang, A. Suresh, C. H. Sharma, M. Thalakulam and M. M. Shaijumon, Nb $_2$ O $_5$/Graphene Nanocomposites for Electrochemical Energy Storage, *RSC Adv.*, 2015, **5**(74), 59997–60004, DOI: **10.1039/C5RA07895D**.

57 X. Wu, W. Hu, J. Qiu, B. Geng, M. Du and Q. Zheng, Solvent-Assisted Self-Assembly to Fabricate a Ternary Flexible Free-Standing Polyaniline@MXene-CNTs Electrode for High-Performance Supercapacitors, *J. Alloys Compd.*, 2022, **921**, 166062, DOI: **10.1016/j.jallcom.2022.166062**.

58 H. Dong, P. Xiao, N. Jin, B. Wang, Y. Liu and Z. Lin, Molten Salt Derived Nb_2CT_xMXene Anode for Li-ion Batteries, *ChemElectroChem*, 2021, **8**(5), 957–962, DOI: **10.1002/celc.202100142**.

59 M. Sanna, K. A. Novčić, S. Ng, M. Černý and M. Pumera, The Unexpected Photoelectrochemical Activity of MAX Phases:

The Role of Oxide Impurities, *J. Mater. Chem. A*, 2023, **11**(6), 3080–3090, DOI: **10.1039/D2TA06929F**.

60 X. Zhang, J. Wang, X. Wang, Y. Li, Y. Zhao, Z. Bakenov and G. Li, 3D Ordered Macroporous Amorphous Nb2O5 as Anode Material for High-Performance Sodium-Ion Batteries, *Appl. Surf. Sci.*, 2021, **567**, 150862, DOI: **10.1016/j.apsusc.2021.150862**.

61 A. C. Nielander, J. M. McEnaney, J. A. Schwalbe, J. G. Baker, S. J. Blair, L. Wang, J. G. Pelton, S. Z. Andersen, K. Enemark-Rasmussen, V. Čolić, S. Yang, S. F. Bent, M. Cargnello, J. Kibsgaard, P. C. K. Vesborg, I. Chorkendorff and T. F. Jaramillo, A Versatile Method for Ammonia Detection in a Range of Relevant Electrolytes via Direct Nuclear Magnetic Resonance Techniques, *ACS Catal.*, 2019, **9**(7), 5797–5802, DOI: **10.1021/acscatal.9b00358**.

62 T. Hu, M. Wang, C. Guo and C. M. Li, Functionalized MXenes for Efficient Electrocatalytic Nitrate Reduction to Ammonia, *J. Mater. Chem. A*, 2022, **10**(16), 8923–8931, DOI: **10.1039/D2TA00470D**.

63 W. Gao, J. V. Perales-Rondon, J. Michalička and M. Pumera, Ultrathin Manganese Oxides Enhance the Electrocatalytic Properties of 3D Printed Carbon Catalysts for Electrochemical Nitrate Reduction to Ammonia, *Appl. Catal., B*, 2023, **330**, 122632, DOI: **10.1016/j.apcatb.2023.122632**.

64 G. Kresse and J. Furthmüller, Efficient Iterative Schemes for *Ab Initio* Total-Energy Calculations Using a Plane-Wave Basis Set, *Phys. Rev. B: Condens. Matter Mater. Phys.*, 1996, **54**(16), 11169–11186, DOI: **10.1103/PhysRevB.54.11169**.

65 G. Kresse and J. Furthmüller, Efficiency of Ab-Initio Total Energy Calculations for Metals and Semiconductors Using a Plane-Wave Basis Set, *Comput. Mater. Sci.*, 1996, **6**(1), 15–50, DOI: **10.1016/0927-0256(96)00008-0**.

66 P. E. Blöchl, Projector Augmented-Wave Method, *Phys. Rev. B: Condens. Matter Mater. Phys.*, 1994, **50**(24), 17953–17979, DOI: **10.1103/PhysRevB.50.17953**.

67 G. Kresse and D. Joubert, From Ultrasoft Pseudopotentials to the Projector Augmented-Wave Method, *Phys. Rev. B: Condens. Matter Mater. Phys.*, 1999, **59**(3), 1758–1775, DOI: **10.1103/PhysRevB.59.1758**.

68 J. P. Perdew, K. Burke and M. Ernzerhof, Generalized Gradient Approximation Made Simple, *Phys. Rev. Lett.*, 1996, **77**, 3865; *Phys. Rev. Lett.*, 1997, **78**, 1396.

69 S. Grimme, J. Antony, S. Ehrlich and H. Krieg, A Consistent and Accurate *Ab Initio* Parametrization of Density Functional Dispersion Correction (DFT-D) for the 94 Elements H-Pu, *J. Chem. Phys.*, 2010, **132**(15), 154104, DOI: **10.1063/1.3382344**.

70 K. Mathew, R. Sundararaman, K. Letchworth-Weaver, T. A. Arias and R. G. Hennig, Implicit Solvation Model for Density-Functional Study of Nanocrystal Surfaces and Reaction Pathways, *J. Chem. Phys.*, 2014, **140**(8), 084106, DOI: **10.1063/1.4865107**.

71 H. J. Monkhorst and J. D. Pack, Special Points for Brillouin-Zone Integrations, *Phys. Rev. B*, 1976, **13**(12), 5188–5192, DOI: **10.1103/PhysRevB.13.5188**.

72 J. K. Nørskov, J. Rossmeisl, A. Logadottir, L. Lindqvist, J. R. Kitchin, T. Bligaard and H. Jónsson, Origin of the Overpotential for Oxygen Reduction at a Fuel-Cell Cathode, *J. Phys. Chem. B*, 2004, **108**(46), 17886–17892, DOI: **10.1021/jp047349j**.

73 V. Wang, N. Xu, J.-C. Liu, G. Tang and W.-T. Geng, VASPKIT: A User-Friendly Interface Facilitating High-Throughput Computing and Analysis Using VASP Code, *Comput. Phys. Commun.*, 2021, **267**, 108033, DOI: **10.1016/j.cpc.2021.108033**.

74 J.-X. Liu, D. Richards, N. Singh and B. R. Goldsmith, Activity and Selectivity Trends in Electrocatalytic Nitrate Reduction on Transition Metals, *ACS Catal.*, 2019, **9**(8), 7052–7064, DOI: **10.1021/acscatal.9b02179**.

75 X. Gao and E. C. M. Tse, Unraveling the Performance Descriptors for Designing Single-Atom Catalysts on Defective MXenes for Exclusive Nitrate-To-Ammonia Electrocatalytic Upcycling, *Small*, 2024, **20**(11), 2306311, DOI: **10.1002/smll.202306311**.

76 J. Hu, S. Osella, E. A. dos Reis, A. B. da Silva, C. Ribeiro, L. H. Mascaro, J. Albero and H. Garcia, Mixed Fe-Mo Carbide Prepared by a Sonochemical Synthesis as Highly Efficient Nitrate Reduction Electrocatalyst, *Appl. Catal., B*, 2024, **357**, 124247, DOI: **10.1016/j.apcatb.2024.124247**.

77 L. Li, X. Wang, H. Guo, G. Yao, H. Yu, Z. Tian, B. Li and L. Chen, Theoretical Screening of Single Transition Metal Atoms Embedded in MXene Defects as Superior Electrocatalyst of Nitrogen Reduction Reaction, *Small Methods*, 2019, **3**(11), 1900337, DOI: **10.1002/smtd.201900337**.